



저작자표시-비영리-변경금지 2.0 대한민국

이용자는 아래의 조건을 따르는 경우에 한하여 자유롭게

- 이 저작물을 복제, 배포, 전송, 전시, 공연 및 방송할 수 있습니다.

다음과 같은 조건을 따라야 합니다:



저작자표시. 귀하는 원저작자를 표시하여야 합니다.



비영리. 귀하는 이 저작물을 영리 목적으로 이용할 수 없습니다.



변경금지. 귀하는 이 저작물을 개작, 변형 또는 가공할 수 없습니다.

- 귀하는, 이 저작물의 재이용이나 배포의 경우, 이 저작물에 적용된 이용허락조건을 명확하게 나타내어야 합니다.
- 저작권자로부터 별도의 허가를 받으면 이러한 조건들은 적용되지 않습니다.

저작권법에 따른 이용자의 권리는 위의 내용에 의하여 영향을 받지 않습니다.

이것은 [이용허락규약\(Legal Code\)](#)을 이해하기 쉽게 요약한 것입니다.

[Disclaimer](#)

Thesis for the Degree of Master of Engineering

Study on improvement of 6SV LUT
discontinuity using DNN: based on
KOMPSAT-3/3A



Division of Earth Environmental System Science
(Major of Spatial Information Engineering)

The Graduate School
Pukyong National University

February 2021

Study on improvement of 6SV LUT
discontinuity using DNN: based on
KOMPSAT-3/3A

(DNN을 활용한 6SV LUT 불연속면
개선 연구: KOMPSAT-3/3A 기반으로)

Advisor: Prof. Kyung-Soo Han

by
Daeseong Jung

A thesis submitted in partial fulfillment of the requirements
for the degree of

Master of Engineering

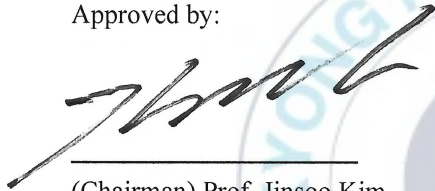
in Department of Spatial Information Engineering, The Graduate School,
Pukyong National University

February 2021

Study on improvement of 6SV LUT discontinuity using DNN:
based on KOMPSAT-3/3A

A dissertation
by
Daeseong Jung

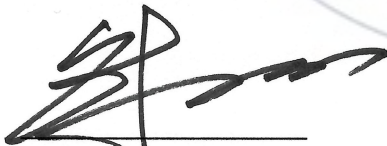
Approved by:



(Chairman) Prof. Jinsoo Kim



(Member) Prof. Chul-Uong Choi



(Member) Prof. Kyung-Soo Han

February 19, 2021

CONTENTS

CONTENTS	i
LIST OF FIGURES.....	iii
LIST OF TABLES.....	vi
LIST OF ACRONYMS	vii
1. Introduction	1
1.1. Background.....	1
2. Study area and Data.....	8
2.1. Study area	8
2.2. Satellite data	9
2.2.1. KOMPSAT-3/3A data.....	9
2.2.2. MODIS data	12
2.2.3. ECMWF data.....	13
3. Methodology.....	15
3.1. Synthesis methodology.....	15
3.2. 6SV RTM	17
3.3. Construction of 6SV LUT	19
3.4. Optimization of LUT.....	21
3.5. DNN model generation	24
3.6. Performance comparison analysis with interpolation methods.....	27
4. Results.....	31

4.1. Generation of an optimized LUT	31
4.2. Evaluation of the DNN model.....	35
4.3. Evaluation of surface reflectance	41
4.3.1. Accuracy comparison	41
4.3.2. Calculation speed comparison.....	46
4.3.3. Analysis of discontinuities	47
5. Summary and Conclusions	49
6. References	51

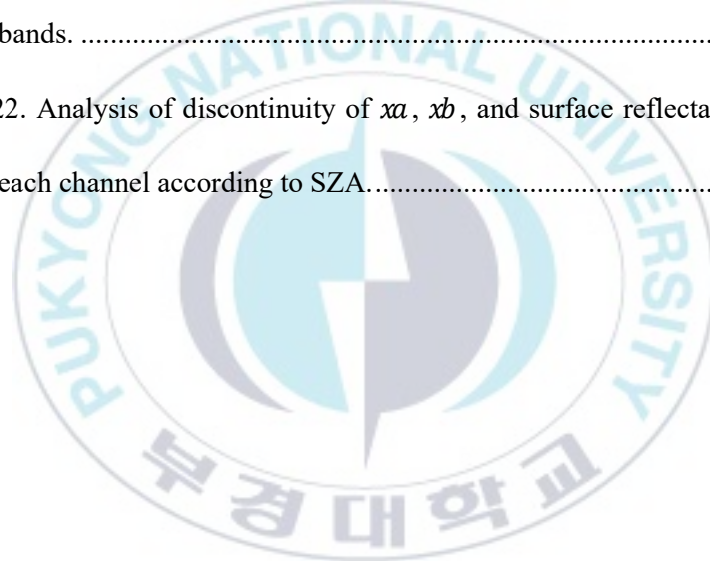


LIST OF FIGURES

Fig. 1. Example of discontinuity in LUT-based surface reflectance.....	6
Fig. 2. LUT-based surface reflectance in satellite imagery (Figure from Lee et al., 2020).....	6
Fig. 3. Examples of surface reflectance of high-resolution images. (a) The surface reflectance calculated based on a single atmospheric component data, (b) the surface reflectance calculated based on not a single atmospheric component data, (c) Surface reflectance calculated as the absolute error between (a) and (b).	7
Fig. 4. The study area and location of satellite images.	8
Fig. 5. SRF for Blue, Green, Red, NIR bands of KOMPSAT-3/3A.	10
Fig. 6. Flowchart of this study	16
Fig. 7. Changes in atmospheric correction coefficients according to SZA and AOD conditions for Blue ((a), (e), (i)), Green((b), (f), (j)), Red ((c), (g), (k)), NIR((d), (h), (l)) bands. The first, second, and third rows represent the coefficients x_a , x_b , and x_c , respectively.	23

Fig. 8. Distribution of random atmospheric components and angular information for performance evaluation. (a) SZA, (b) RAA, (c) VZA, (d) TPW, (e) TCO, (f) AOD.....	30
Fig. 9. The average of RMSE for coefficients α , β of each band based on DNN. MS1 ((a), (e)), MS2 ((b), (f)), MS3 ((c), (g)), MS4 ((d), (h)) bands. The first and second rows represent the coefficients α and β , respectively.	33
Fig. 10. The rate of change of coefficients α and β for each band in the AOD (1.0-5.0) range in Table 3. (a) The rate of change of coefficients α , (b) the rate of change of coefficients β	34
Fig. 11. (a) Table 3 based DNN model estimation results, (b) optimized LUT based DNN model estimation results	34
Fig. 12. Scatter plot of DNN α and 6SV α for each band.	36
Fig. 13. Scatter plot of LUT α and 6SV α for each band.....	36
Fig. 14. Scatter plot of MCS α and 6SV α for each band.	37
Fig. 15. Scatter plot of 6D α and 6SV α for each band.....	37
Fig. 16. Scatter plot of DNN β and 6SV β for each band.....	38
Fig. 17. Scatter plot of LUT β and 6SV β for each band.....	38


Fig. 18. Scatter plot of MCS x_b and 6SV x_b for each band.	39
Fig. 19. Scatter plot of 6D x_b and 6SV x_b for each band.....	39
Fig. 20. Average of RMSE for surface reflectance of DNN, LUT, MCS, 6D according to SZA interval. (a) Blue, (b) Green, (c) Red (d) NIR bands.	44
Fig. 21. Average of RMSE for surface reflectance of DNN, LUT, MCS, 6D according to AOD interval. (a) Blue, (b) Green, (c) Red, (d) NIR bands.	45
Fig. 22. Analysis of discontinuity of x_a , x_b , and surface reflectance for each channel according to SZA.....	48



LIST OF TABLES

Table 1. Specifications of KOMPSAT-3/3A	10
Table 2. Information on images of KOMPSAT-3/3A used in the study	11
Table 3. Range and interval of input parameters used for LUT construction	20
Table 4. Hyper parameters of the model used to generate an optimal model	25
Table 5. Validation data used when training a DNN-based model	26
Table 6. DNN, LUT, MCS, and 6D accuracy evaluation for coefficients of each band	40
Table 7. DNN, LUT, MCS, and 6D accuracy evaluation for coefficients of each band	40
Table 8. Average of RMSE for surface reflectance of each channel based on DNN, LUT, MCS, 6D	43
Table 9. Time it takes to calculate surface reflectance from one satellite imagery of 6SV, DNN, LUT, MCS, 6D	47

LIST OF ACRONYMS



AOD	Aerosol Optical Depth
CAMS	Copernicus Atmosphere Monitoring Service
DNN	Deep Neural Network
ECMWF	European Center for Medium-Range Weather Forecasts
KARI	Korea Aerospace Research Institute
KOMPSAT-3/3A	Korea Multi-Purpose SATellite-3/3A
LibRadtran	Library for Radiative transfer
LUT	Look-up table
MACC	Monitoring Atmospheric Composition and Climate
MCS	Minimum Curvature Surface
MODIS	Moderate Resolution Imaging Spectroradiometer
MODTRAN	MODerate resolution atmospheric TRANsmission
MS	Multispectral
NIR	Near-Infrared
NRT	Near-real time
PAN	Panchromatic

RAA	Relative Azimuth Angle
RMSE	Root Mean Square Error
RRMSE	Relative Root Mean Square Error
RTM	Radiative Transfer Model
SRF	Spectral Response Function
Suomi-NPP	Suomi National Polar-orbiting Partnership
SZA	Solar Zenith Angle
TCO	Total Column Ozone
TOA	Top of the atmosphere
TPW	Total Precipitable Water
VIIRS	Visible Infrared Imaging Radiometer Suite
VZA	Viewing Zenith Angle
6D	Six-Dimensional linear interpolation
6SV	Second Simulation of a Satellite Signal in the Solar Spectrum Vector

DNN을 활용한 6SV LUT 불연속면 개선 연구:
KOMPSAT-3/3A 기반으로

정 대 성

부 경 대 학 교 대 학 원 공 간 정 보 시 스 템 공 학 과

요 약

대기보정은 대기효과를 제거하여 지표반사도를 산출하는 방법이다. 식생지수 등 위성 기반의 2 차 산출물들을 획득하기 위하여 정확한 대기보정 방법은 필수적이다. 복사전달모델은 정확도는 높지만, 연산 과정에 많은 시간이 소요된다. 이를 해결하기 위하여 조건표 기반 실시간 지표반사도를 산출하고 있다. 그러나, 조건표 구축에 사용되는 입력 변수들의 간격으로 인해 지표반사도를 산출하는 과정에서 불연속면이 발생한다. 즉, 지표반사도의 오차를 발생시켜 정확한 지표에 대한 정보를 획득하기가 어렵다. 조건표의 간격을 해소하기 위하여 선행 연구들은 조건표에 보간법을 적용하고 있다. 보간법을 통해 지표반사도의 정확도는 향상되었지만, 태양 천정각, 에어로졸 등 지표반사도 산출 과정에 영향력이 큰 입력 변수들의 변동성을 해결하기에는 한계가 있다. 이 한계점을 해결하기 위하여, Deep Neural Network (DNN) 기반 지표반사도 산출 모델을 생성하였다. DNN 모델은 비선형 관계들을 모델링하여 예측 모델을 생성하고, 연산에 대한 효율도 높게 나타나고 있다. 그리고, 기존의 고해상도 영상에 대해 대기보정 수행 시 단일 대기 성분 자료를 입력하여 지표반사도를 산출하였다. 이것은 고해상도 영상의 정밀한 지표반사도를 산출하는 방법에 적합하지 않다. 본 연구는 고해상도 위성인 다목적실용위성-3/3A 호의 지표반사도를 산출하기 위하여 연구를 수행하였다. DNN 모델의 성능을 평가하기 위하여 보간법 대비 정확도 및 산출 속도에 대하여 분석하였다. DNN 모델은 보간법의 정확도 대비 복사전달모델과 유사한 결과가 나타났고, 산출 속도도 조건표와 차이가 없는 결과가 나타났다. 본 연구를 통해 다양한 기하 자료 및 대기 성분에 대해 높은 정확도로 지표반사도를 산출할 수 있다.

1. Introduction

1.1. Background

The satellite's sensor acquires information about the target on the surface by measuring the radiance reflected from the ground surface. In this process, atmospheric molecules and aerosols in the atmosphere layers absorb, scatter, and reflect radiance. Because of these atmospheric components, the at-sensor radiance has an error. This effect is called the atmospheric effect, and the process of retrieving the surface reflectance by removing the atmospheric effect is called atmospheric correction (Liang et al., 2001). Therefore, to obtain precise information of the target on the surface, a precise atmospheric correction method is essential in the pre-processing of satellite images.

Previous studies performed atmospheric correction using physically based Radiative Transfer Model (RTM) such as the Second Simulation of a Satellite Signal in the Solar Spectrum vector (6SV) (Vermote et al., 2006), MODerate resolution atmospheric TRANsmission (MODTRAN) (Berk et al., 2006), and Library for Radiative transfer (LibRadtran) (Mayer and Kylling, 2005). The RTM accounts for radiance in the atmosphere by using the Spectral Response Function (SRF) of the sensor, angular

information (Solar Zenith Angle; SZA, Relative Azimuth Angle; RAA, Viewing Zenith Angle; VZA, and other angular information), and atmospheric components (Total Precipitable Water; TPW, Total Column Ozone; TCO, Aerosol Optical Depth; AOD, and other atmospheric components). In addition, the accuracy of RTM is high because it uses data that have same characteristics as the spatial and temporal information of satellite images.

However, the calculation process of RTM is time consuming. It is difficult to apply it to the retrieval of real-time surface reflectance in satellite images. To overcome for this limitation, studies related to atmospheric correction used a Look-up table (LUT) that stores pre-calculated output values of RTM to perform an array indexing operation. This method improved the processing efficiency of surface reflectance retrieval (Liang et al., 2001; Lyapustin et al., 2011). Nevertheless, since the input parameters of the LUT are constructed with an interval, the accuracy is low when retrieval of the surface reflectance for angular information and atmospheric components existing within the interval (Qu et al., 2013). In other words, discontinuity in surface reflectance occurs in satellite images (Fig. 1, Fig. 2). To improve the accuracy of the surface reflectance retrieved based on the LUT, previous studies improved the LUT by applying interpolation methods (Staenz et al., 2002, Liang et al.,

2006). Although interpolation methods have improved the accuracy of the surface reflectance, the error of the surface reflectance is still increasing as SZA the higher (Lee et al., 2020). This is because the higher the SZA, the longer the atmospheric path of radiance. In other words, radiance is highly affected by atmospheric effects and the variability of the surface reflectance increases (Vermote et al., 2006). It is difficult to improve this variability with interpolation methods. In addition, since AOD, an important input parameter in the atmospheric correction process, has a large weight on the atmospheric effect, the surface reflectance is also sensitive to AOD (Boehmle et al., 2018).

Atmospheric correction algorithms of Moderate Resolution Imaging Spectroradiometer (MODIS) and Visible Infrared Imaging Radiometer Suite (VIIRS) set the upper limit of AOD up to 5.0 and retrieve the surface reflectance based on LUT (Vermote et al., 2011). However, there are insufficient studies to retrieve and analyze LUT-based surface reflectance by setting the upper limit of AOD to 5.0. Namely, it is necessary to consider the influence of atmospheric effects that appear as the values of the input parameters increase, and to improve the discontinuities that appear in the process of retrieving the surface reflectance based on LUT.

In this study, we propose a Deep Neural Network (DNN) as a method that can calculate real-time surface reflectance while improving the

discontinuity of LUT. The DNN consists of several layers hidden between the input and output layers, allowing you to model complex nonlinear relationships between input and output values (Schmidhuber, 2015). This has the advantage of generating a model that produces an output with high accuracy by training input data and has good computational efficiency (Al-Jarrah et al., 2015). For this reason, recently, study on producing satellite data-based outputs using DNN in the field of remote sensing has been conducted. (Yeom et al., 2019; Ma et al., 2020). In this study, DNN trained LUT constructed with RTM to improve discontinuities and generated a model capable of calculating surface reflectance for various angular information and atmospheric components.

The satellite image data used in the study is Korea Multi-Purpose SATellite-3/3A (KOMPSAT-3/3A), which provides high-resolution images with a spatial resolution of about 2m (visible and near infrared bands). Unlike low and medium-resolution satellites such as Terra/Aqua and Suomi National Polar-orbiting Partnership (Suomi-NPP) that provide atmospheric correction outputs, high-resolution satellite imagery does not provide atmospheric correction outputs. This is because high-resolution satellite images have been widely used as visual data such as map making (Vu et al., 2010). In general, when performing atmospheric corrections on high-resolution images, a single pixel atmospheric component data was

applied to all pixels in the image. When a variety of atmospheric components is observed in a high-resolution image, an error in surface reflectance occurs in the conventional method (Fig. 3). Therefore, Not applying a single atmospheric component data obtains precise surface reflectance in high-resolution images.

The purpose of this study is to calculate an accurate surface reflectance by improving the discontinuity of the LUT using DNN. We constructed the LUT of KOMPSAT-3/3A using 6SV RTM, which is currently open source, and the LUT is provided as training data to generate an atmospheric correction model that automatically calculates surface reflectance by DNN. Then, the performance of the DNN-based model was analyzed by comparing the DNN-based surface reflectance with the interpolated surface reflectance.

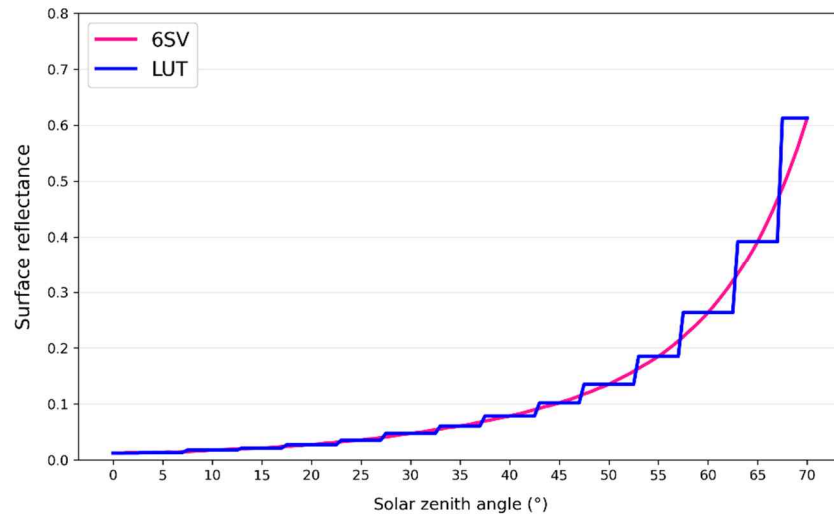


Fig. 1. Example of discontinuity in LUT-based surface reflectance.

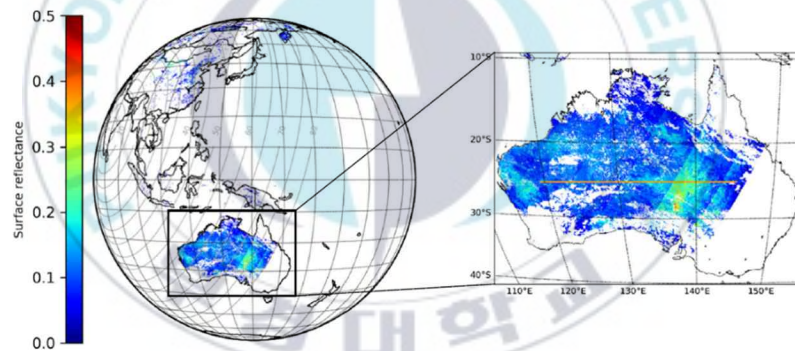


Fig. 2. LUT-based surface reflectance in satellite imagery (Figure from Lee et al., 2020).

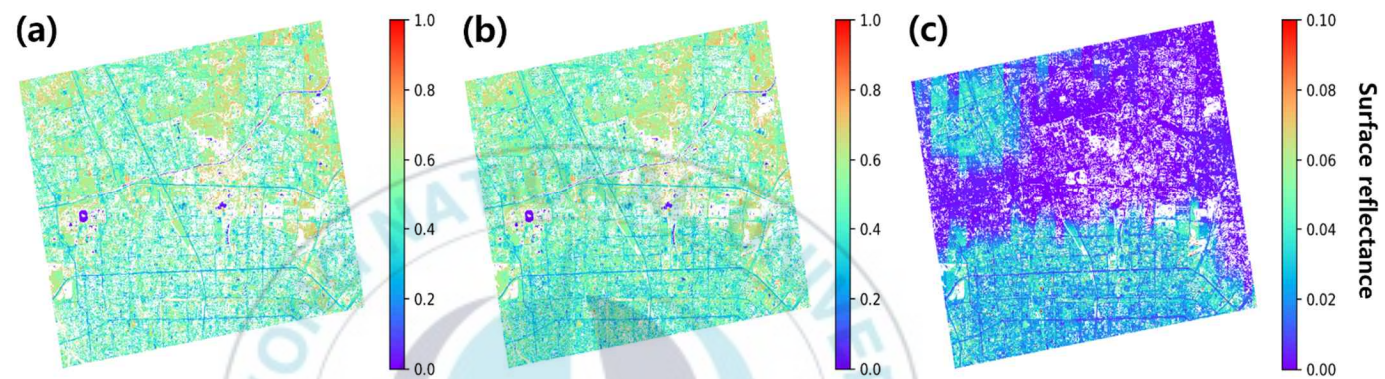


Fig. 3. Examples of surface reflectance of high-resolution images. (a) The surface reflectance calculated based on a single atmospheric component data, (b) the surface reflectance calculated based on not a single atmospheric component data, (c) Surface reflectance calculated as the absolute error between (a) and (b).

2. Study area and Data

2.1. Study area

The study area is land included in 20°N-50°N, 100°E-130°E (Fig. 4). This area has a variety of surface land types and climate types (Corlett, 2014). In addition, it is an area where the variability of aerosols concentration is large due to the yellow dust occurring in the desert (Wang et al., 2008).

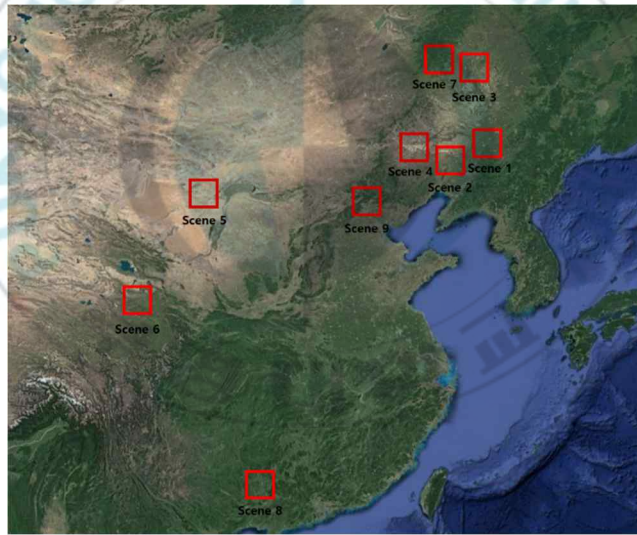


Fig. 4. The study area and location of satellite images.

2.2. Satellite data

2.2.1. KOMPSAT-3/3A data

KOMPSAT-3 and KOMPSAT-3A were launched for the purpose of Earth observation on May 18, 2012 and March 25, 2015, respectively. KOMPSAT-3/3A are polar orbit satellites that are operated by Korea Aerospace Research Institute (KARI) and provide sub-meter resolution (Panchromatic band). KOMPSAT-3A is the sister of KOMPSAT-3, except for the Near-Infrared (NIR) band that KOMPSAT-3A has, their spectral bands are the same. That is, the visible and NIR bands of KOMPSAT-3/3A have the same SRF (Fig. 5). Table 1 shows the specification of KOMPSAT-3/3A.

Table 2 shows information about KOMPSAT-3/3A images (Scene 1–9) shown in Fig. 4, and these information describe the date, time, and area when the images were observed. KOMPSAT-3/3A images used in this study are Level 1G products to which radiometric correction, sensor correction and geometric distortions correction are applied. These images were cloud-free, and blue, green, red, and NIR bands were used in the study.

Table 1. Specifications of KOMPSAT-3/3A

Parameter	KOMPSAT-3	KOMPSAT-3A
Altitude	685 km	528 km
Wavelength	Pan: 0.45-0.90 μm Blue: 0.45-0.52 μm Green: 0.52-0.60 μm Red: 0.63-0.69 μm NIR: 0.76-0.90 μm	Pan: 0.45-0.90 μm Blue: 0.45-0.52 μm Green: 0.52-0.60 μm Red: 0.63-0.69 μm NIR: 0.76-0.90 μm IR: 3.3-5.2 μm
Spatial resolution	Pan: 0.7 m MS: 2.8 m	Pan: 0.55 m MS: 2.2 m IR: 5.5 m
Swath width	15 km (at nadir)	12 km (at nadir)

Pan: Panchromatic, *MS*: Multispectral (MS1: Blue, MS2: Green, MS3: Red, MS4: NIR)

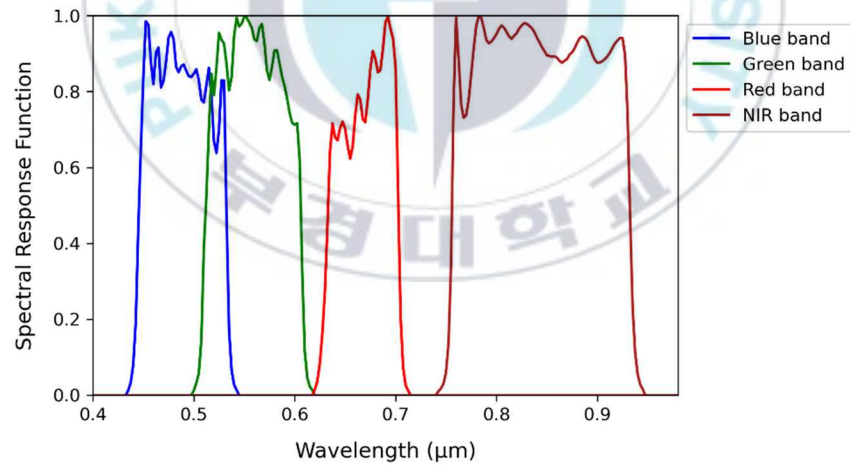


Fig. 5. SRF for Blue, Green, Red, NIR bands of KOMPSAT-3/3A.

Table 2. Information on images of KOMPSAT-3/3A used in the study

Satellite	Scene number	Date	Time (UTC)	Center latitude	Center longitude
KOMPSAT-3	Scene 1	2015-09-06	04:28:51	43.05°N	124.43°E
	Scene 2	2016-04-05	04:54:00	42.22°N	123.08°E
KOMPSAT-3A	Scene 3	2016-12-02	05:00:27	46.99°N	123.75°E
	Scene 4	2018-02-21	05:01:16	42.73°N	120.17°E
	Scene 5	2018-03-14	06:00:46	40.57°N	105.81°E
	Scene 6	2018-04-07	06:26:32	34.77°N	101.05°E
	Scene 7	2018-08-20	04:42:39	47.01°N	123.68°E
	Scene 8	2018-10-05	05:56:01	24.36°N	109.58°E
	Scene 9	2019-05-20	05:26:31	40.02°N	116.37°E

2.2.2. MODIS data

We used atmospheric component data from MODIS operating in Terra/Aqua satellites. This is because KOMPSAT-3/3A does not retrieve atmospheric component data. We used MODIS Atmospheric Profiles (MODIS/Terra Temperature and Water Vapor Profiles 5-Min L2 Swath 5 km; MOD07, MODIS/Aqua Temperature and Water Vapor Profiles 5-Min L2 Swath 5 km; MYD07) and MODIS Aerosol Product (MODIS/Terra Aerosol 5-Min L2 Swath 3 km; MOD04_3K, MODIS/Aqua Aerosol 5-Min L2 Swath 3 km; MYD04_3K) among MODIS level-2 products as data for atmospheric correction.

The MODIS Atmospheric Profiles (MOD07, MYD07) provides several parameters, including TCO, TPW, moisture profile. This product generated day and night when at least nine field of views are cloud-free and provide a daily atmospheric profile at 5 km spatial resolution. The MODIS Aerosol Product (MOD04_3K, MYD04_3K) provides AOD, aerosol size distribution, and other parameters. This product is produced based on the Dark Target aerosol algorithm and is generated daily at 3 km spatial resolution to evaluate air quality in the high-scale area. We used TPW and TCO of MODIS Atmospheric Profiles (MOD07, MYD07) and AOD of MODIS Aerosol Product (MOD04_3K, MYD04_3K) in the process of performing atmospheric correction of KOMPSAT-3/3A data.

The MODIS data has the closest time to the time when the image was acquired by KOMPSAT-3/3A. Also, match-up was performed due to the difference in spatial resolution between KOMPSAT-3/3A data and MODIS data.

2.2.3. ECMWF data

The European Center for Medium-Range Weather Forecasts (ECMWF) is conducting numerical weather prediction studies to produce accurate climate data and medium-range forecasts. ECMWF operates The Copernicus Atmosphere Monitoring Service (CAMS) service under the European Union's Copernicus Earth observation programme. The CAMS provides information on the composition and variability of atmospheric components based on models and observation data from sources such as satellites and in-situ sensors. The CAMS Near-real time (NRT) provides daily analysis and prediction of atmospheric composition and aerosol concentrations related to climate change. This assimilation system is based on the Integrated Prediction System and has a 4D variation analysis. This system was generated by the Monitoring Atmospheric Composition and Climate (MACC) study (Koffi and Bergamaschi, 2018). So, The MACC reanalysis is a data of atmospheric composition provided by CAMS, and the data are from 2003 to 2012.

In this study, there are cases where it is impossible to perform atmospheric correction due to the missing value of MODIS data. To prevent this case, climate values (TPW, TCO, AOD) were generated based on data of CAMS NRT and MACC reanalysis (not missing value). Considering the operating period of KOMPSAT-3/3A and the minimum synthetic period recommended for constructing a climate dataset, the data period was set as from 2010 to 2019. In the case of CAMS, data are provided from July 2012, so the data for 2010-2012 considered the MACC. To confirm the difference between the two data, the daily average value (0.125° of spatial resolution, respectively) from July to December 2012, which is the common period between the two data, was compared and analyzed. Here, the analysis area was set as 15°N - 55°N , 70°E - 145°E considering the study area (Fig. 4). The comparative analysis result of CAMS and MACC data confirmed that there was little difference between the data (Root Mean Square Error; RMSE = 0.0125 g/cm^2 and bias = -0.0074 g/cm^2 for TPW, and RMSE = 0.0061 cm-atm and bias = -0.006 cm-atm for TCO, and RMSE = 0.0295 and bias = -0.0197 for AOD). This result was judged to have little influence on the method of generating climate values and calculating surface reflectance in this study. The monthly average climate value was constructed based on MACC and CAMS data.

3. Methodology

3.1. Synthesis methodology

Fig. 6 shows the synthesis methodology process of this paper. First, a 6SV-based LUT was constructed to make training data to be provided to DNN. After that, the DNN trained the LUT to generate a model for retrieving the surface reflectance, and the generated DNN model estimated the intermediate values of the LUT. Based on the predicted results, the interval of the LUT, which shows a high error, was finely reconstructed, and the intermediate value of the LUT was again estimated. To evaluate the performance of the reconstructed LUT-based DNN model, the interpolation methods used in previous studies were compared and analyzed based on three criteria (accuracy, discontinuity, retrieval speed). In this analysis, 6SV was used as verification data.

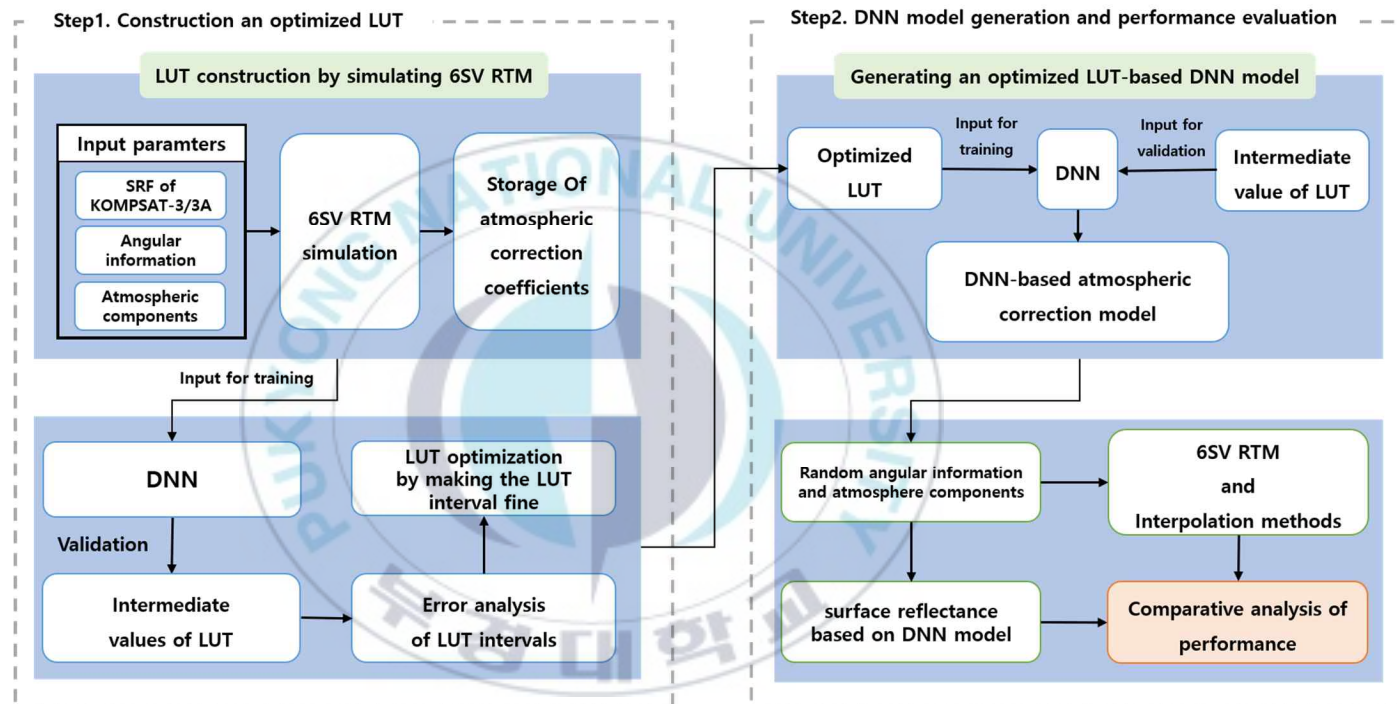


Fig. 6. Flowchart of this study

3.2. 6SV RTM

The 6SV RTM was used to construct a LUT for KOMPSAT-3/3A. The 6SV is a vector version with improved accuracy in 6S (scalar version) (Vermote et al., 1997). Whereas the 6SV accounts for the polarization effect, the previous version 6S ignored the polarization effect. In addition, the number of scattering angles used to set the scattering phase function in 6SV has increased, and conditions of the vertical aerosol profile can be finely set. 6SV has higher simulation accuracy than other RTMs such as MODTRAN and SHARM (Kotchenova et al., 2006). Therefore, many studies have used 6SV to correct atmospheric effects in studies such as radiometric calibration (Yeom et al., 2018) and retrieval of aerosol (Ignatov et al., 2002), as well as studies on retrieving surface reflectance.

The 6SV calculates atmosphere components, angular information, and SRF of the sensor to retrieve atmospheric correction coefficients (x_a, x_{ap}, x_b , and x_c). Among these coefficients, x_{ap} is used to calculate the surface reflectance based on the Top of the atmosphere (TOA) reflectance of satellite data. However, the TOA radiance from satellite data is used to retrieve the surface reflectance in this study. Therefore, coefficients (x_a, x_b , and x_c) were used excluding the coefficient x_{ap} in the process of this study.

And, the SRF of the band is calculated by dividing the band width of the sensor by 2.5nm by 6SV. The equation (1), (2), and (3) describe the atmospheric correction coefficients, respectively. xa means the inverse of transmittance, T_g is the gaseous transmission of H2O, CO2, O2, O3 for radiance. θ_s, θ_v are the SZA, VZA, respectively. $T^\downarrow(\theta_s)$ is the total transmission of the atmosphere in the path between the sun and the surface. $T^\uparrow(\theta_v)$ is the atmospheric transmittance occurring in the radiance path between the satellite sensor and the surface. xb represents the scattering term of the atmosphere, and ρ_{R+A} is the reflectance of molecule and aerosol in the atmospheric layer. $xc (= S)$ represents the reflectance of the atmosphere for isotropic light (spherical albedo).

$$xa = \frac{1}{T_g(\theta_s, \theta_v) T^\downarrow(\theta_s) T^\uparrow(\theta_v)} \quad (1)$$

$$xb = \frac{\rho_{R+A}}{T^\downarrow(\theta_s) T^\uparrow(\theta_v)} \quad (2)$$

$$xc = S \quad (3)$$

The surface reflectance is retrieved by applying the atmospheric correction coefficients to the radiance as shown in the following equation (4). L is the measured TOA radiance and ρ_{TOC} is the surface reflectance corrected for the atmospheric effect.

$$\rho_{TOC} = \frac{xa \times L - xb}{1 + xc \times (xa \times L - xb)} \quad (4)$$

3.3. Construction of 6SV LUT

Table 3 shows information on input parameters used in 6SV simulation for LUT generation in this study. The input parameters to be used for LUT construction and the range and interval of input parameters were determined by referring to previous studies (Liang et al., 2010; Lee et al., 2020). The atmospheric correction algorithm of MODIS, VIIRS, and Landsat satellites designed an upper limit of 75° for SZA (Vermote et al., 2011), but this study set an upper limit of 80° for SZA to analyze LUT sensitivity and performance of DNN models. In addition, since many errors occur largely in $\text{SZA} > 70^\circ$ (Lee et al., 2020), it was constructed with 5° intervals in the SZA 0° - 70° range, and 2° intervals in the SZA 70° - 80° range. Unlike other parameters with regular intervals, AOD has 16 values with irregular intervals. In addition, an aerosol type was used as continental to correct the atmosphere on land, and the surface type was assumed to be a vegetation type with homogeneous Lambertian reflectance. We calculated the atmospheric correction coefficients by using 6SV for all combinations shown in table 3. The calculated atmospheric correction coefficients were stored as the output of the LUT with a six-dimensional structure. Four LUTs were generated for each band. In Fig. 5, since the SRFs of KOMPSAT-3 and 3A are identical to each

other, it is possible to calculate the surface reflectance of KOMPSAT-3 and 3A using one LUT.

Table 3. Range and interval of input parameters used for LUT construction

Parameter	Min	Max	Interval
Solar Zenith Angle (°)	0	80	5 (0-70) / 2 (70-80)
Relative Azimuth Angle (°)	0	180	10
Viewing Zenith Angle (°)	0	30	5
Total Precipitable Water (g/cm ²)	0	3	0.5
Total Column Ozone (atm-cm)	0.25	0.35	0.05
Aerosol Optical Depth	0.01, 0.05, 0.1, 0.15, 0.2, 0.3, 0.4, 0.6, 0.8, 1.0, 1.5, 2.0, 2.5, 3.0, 4.0, 5.0		

3.4. Optimization of LUT

Atmospheric components have different sensitivity according to wavelength (Kaufman et al., 1997; Mayer et al., 2016). Among them, because AOD reacts more sensitively as the wavelength of the band becomes shorter, it greatly increases the error of the surface reflectance (Vermote et al., 2011). Fig. 7 Shows the change of atmospheric correction coefficients according to the change of SZA and AOD in the LUT constructed in section 3.3 (RAA: 90°; VZA: 15°; TPW: 1.5 g/cm²; TCO: 0.3 atm-cm). The value of coefficient α for each band increases significantly at SZA>70° and shows rapid variability as the AOD increases and the wavelength shortens (Fig. 7(a), Fig. 7(b), Fig. 7(c), Fig. 7(d)). We found that SZA was fixed at 80°, and when the AOD value changed from 4.0 to 5.0, the rate of change in coefficient α was about 63.2% in Fig. 7(d) and 123.2% in Fig. 7(a). The change in coefficient β is also shown similarly to the change in coefficient α (Fig. 7(e), Fig. 7(f), Fig. 7(g), Fig. 7(h)). SZA was fixed at 80°, and when the AOD value was changed from 4.0 to 5.0, the rate of change of the coefficient β was about 68.5% in Fig. 7(h) and 137.4% in Fig. 7(e). This shows that LUT

construction for each band should not be performed with the same atmospheric components and angular information. And it is expected that the change of coefficients according to the interval of these input parameters will cause an error when using the DNN model. To solve this error, we analyzed the rate of change and sensitivity of the coefficients stored in the LUT and performed the work to make the rate of change of the coefficient constant. And, coefficient x_c is only affected by AOD among input parameters (Lee et al., 2015). Since it does not have a relationship with other input variables, a DNN model that predicts the coefficient x_c was generated, but it was used only when calculating the surface reflectance.

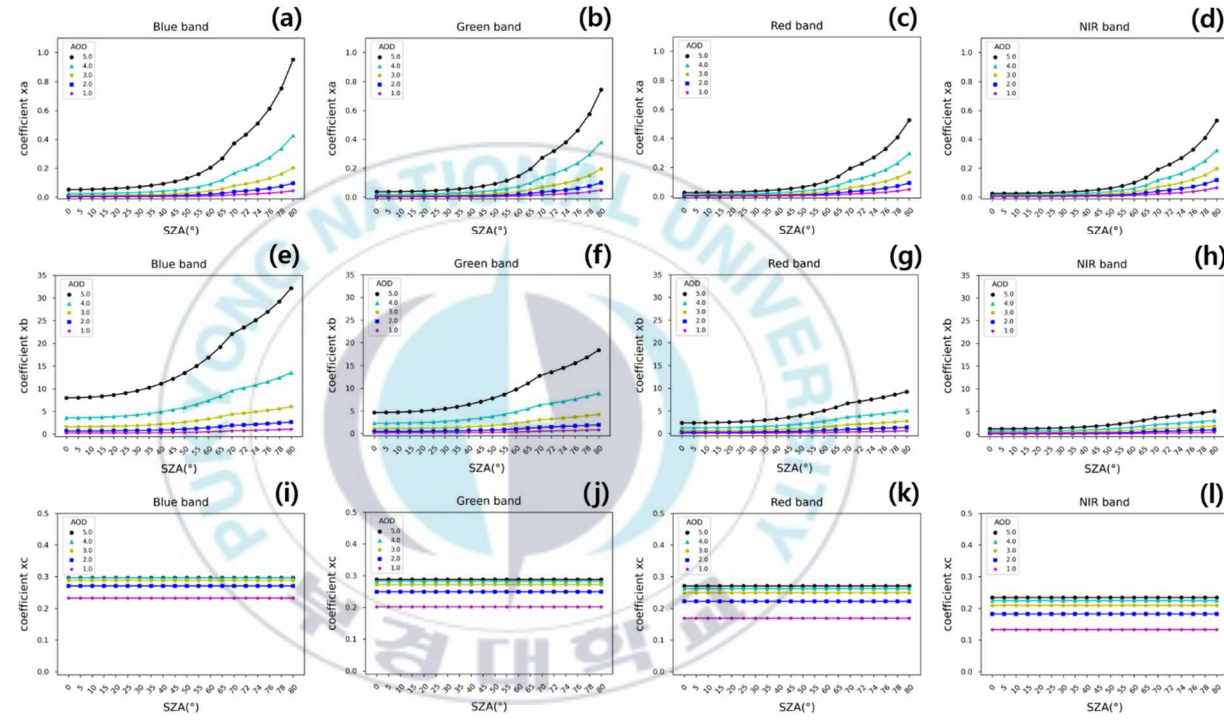


Fig. 7. Changes in atmospheric correction coefficients according to SZA and AOD conditions for Blue ((a), (e), (i)), Green((b), (f), (j)), Red ((c), (g), (k)), NIR((d), (h), (l)) bands. The first, second, and third rows represent the coefficients x_a , x_b , and x_c , respectively.

3.5. DNN model generation

The DNN is a type of neural network modeled with an algorithm that automatically extracts and learns high-dimensional features using a hidden layer (Thomas et al., 2017). DNN uses a feed forward network and error back propagation to adjust the weight and bias of each node in the hidden layers. In this study, the activation function was used a rectified linear unit in the process of making a DNN-based model. The activation function calculates how much input data will be reflected to the next layer. And, rectified linear unit is simple to compute and operate like a linear function, making it easy to optimize the model (Krizhevsky et al., 2017). Since sparse expression is possible, it is efficient in the model learning process. L1 regularization and L2 regularization were used to prevent model overfitting and to improve generalization performance. L1 normalization makes weights close to zero to 0, and L2 regularization is designed to make weights close to zero overall (Cook, 2016). The batch size is the size of the training data used to estimate the error before the model weights are updated. In general, the smaller the batch size, the better the performance of generalization.

In this study, to generate a DNN-based surface reflectance retrieval model, the LUT generated through the optimization process in Section 4.1

was used as training data for DNN. The atmospheric components (TPW, TCO, AOD) and angular information (SZA, RAA, VZA) configured in the optimized LUT were used as input values, and each coefficient was used as an output value. Validation data is required while the DNN is training the optimized LUT. The combinations shown in Table 5 are simulated with 6SV to calculate the coefficients. After that, the atmospheric components and angular information shown in Table 5 and the coefficients calculated by 6SV were used as verification data. In addition, atmospheric components and angular information used when generating a DNN-based model are normalized to 0-1 because the units of values are different.

Table 4. Hyper parameters of the model used to generate an optimal model

Parameter	Value
Node	100, 200, 300
Layer	3, 4, 5
L1 regularization	0, 1×10^{-5} , 1×10^{-6}
L2 regularization	0, 1×10^{-5} , 1×10^{-6}
Batch size	64, 128, 256, 512, 1024

Table 5. Validation data used when training a DNN-based model

Parameter	Min	Max	Interval
Solar Zenith Angle (°)	2.5	79	5 (2.5-67.5)/ 2 (71-79)
Relative Azimuth Angle (°)	5	175	10
Viewing Zenith Angle (°)	2.5	27.5	5
Total Precipitable Water (g/cm ²)	0.25	2.75	0.5
Total Column Ozone (atm-cm)	0.275	0.325	0.05
Aerosol Optical Depth	0.03, 0.075, 0.125, 0.175, 0.25, 0.35, 0.5, 0.7, 0.9, 1.25, 1.75, 2.25, 2.75, 3.5, 4.5		

3.6. Performance comparison analysis with interpolation methods

The performance of the optimized LUT-based DNN model was evaluated using the Minimum Curvature Surface (MCS) interpolation method and Six-Dimensional linear interpolation (6D) used in previous studies. The MCS produces smooth surface from irregularly scattered data (Rabah and Kaloop, 2013). That is, the minimum curvature interpolates the given data and generates a smooth surface while preserving the irregularly distributed data as much as possible. Lee et al. (2020) interpolated SZA and VZA using MCS with 0.5° intervals in order to improve the accuracy of LUT-based surface reflectance in Himawari-8/Advanced Himawari Imager data. In this study, the optimized LUT was interpolated using MCS. The higher the VZA, the greater the error in surface reflectance occurs (Vermote et al., 2011; Lee et al., 2020). However, since the VZA of KOMPSAT-3/3A has a range at a low angle, here the surface reflectance is not significantly influenced by VZA. The AOD was interpolated instead of VZA. Here, the SZA was interpolated with an interval of 0.5° , and AOD was interpolated with 0.05 interval.

The 6D is a method of interpolating by expanding bilinear interpolation into a six-dimensional space (Guanter et al., 2009). Each

value near the interpolation point is weighted by a hyper area expanding the interpolation point to the opposite grid point. The 6D is different from LUT and MCS, which index the output suitable for the input condition while the output of the RTM is stored in advance. The 6D is to extend the linear interpolation processing to six dimensions in an optimized LUT whenever a value of an input parameter is given. Therefore, the accuracy is high, but the interpolation process takes a lot of time. This method is not suitable for the purpose of calculating real-time surface reflectance, but we used 6D to evaluate the accuracy of the optimized LUT-based DNN model.

To evaluate the performance of LUT, MCS, 6D, and DNN, the reference data was used as 6SV. 6SV generated a total of 160,000 reference data by simulating various random angular information and atmospheric components (Fig. 8). In Fig. 8, it is shown that the SZA of the reference data is distributed with 5° intervals from 0° to 80°. One SZA interval has a total of 10,000 data, and the angular information (RAA, VZA) and atmospheric components (TPW, TCO, AOD) are uniformly distributed within this interval. The three performances (accuracy, processing efficiency, discontinuity) of each surface reflectance calculation method were compared and analyzed. In the accuracy comparison analysis, two quantitative analysis methods (RMSE, Relative

Root Mean Square Error; RRMSE) were used to quantitatively evaluate the atmospheric correction coefficients and surface reflectance calculated. At the same time, the calculation speed was checked for the same input data and the efficiency of calculating the surface reflectance was compared. In the discontinuity analysis, the degree to which each method eliminated the discontinuity caused by the interval of the existing LUT was analyzed.



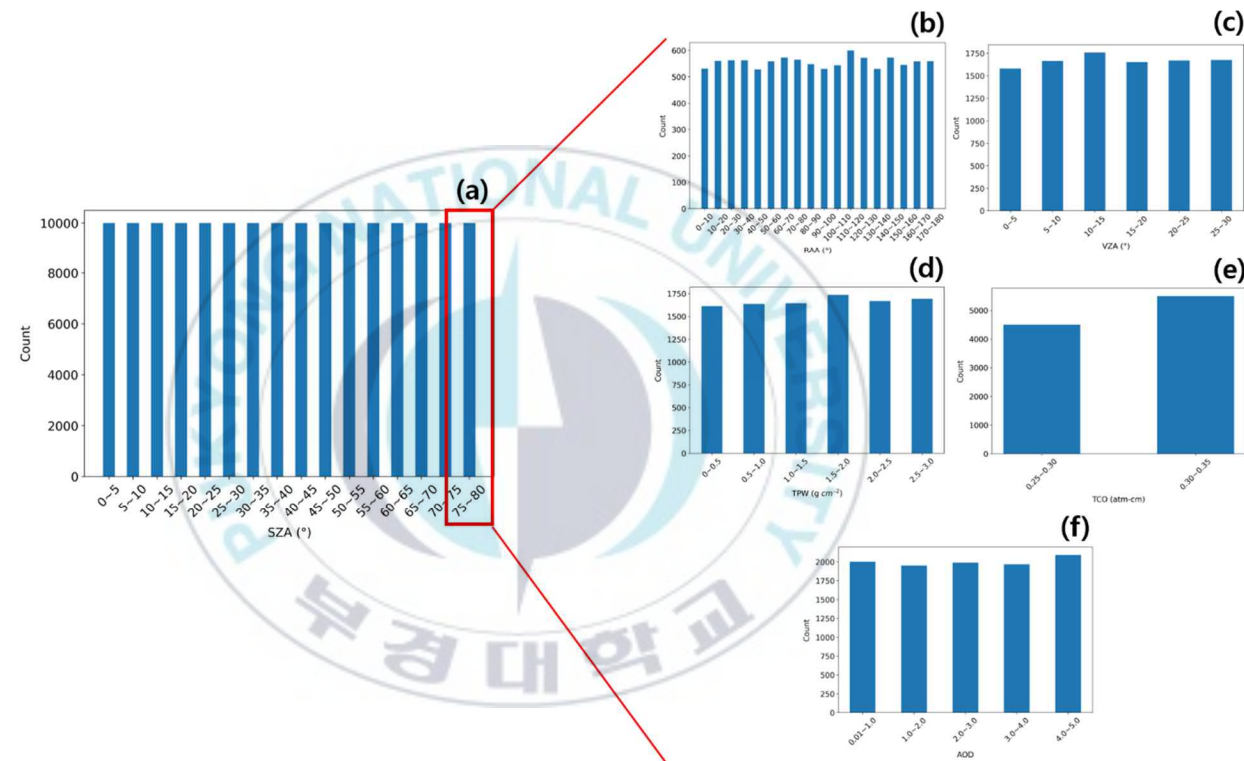


Fig. 8. Distribution of random atmospheric components and angular information for performance evaluation.
(a) SZA, (b) RAA, (c) VZA, (d) TPW, (e) TCO, (f) AOD

4. Results

4.1. Generation of an optimized LUT

Fig. 9 shows the DNN based on Table 3 estimated for Table 5, and the result is calculated as the average of RMSE. It was found that the estimation performance of the DNN model was relatively low in the MS1. Overall, the average of RMSE between models differed significantly due to the difference in the variability of the coefficients. In addition, it was confirmed that all models appeared to be higher than the average of RMSE of each model in the AOD (1.25-4.5) range. To solve this average of RMSE, we optimized the AOD (1.0-5.0) range in Table 3 to be fine.

Fig. 10 shows the rate of change of the coefficients α and β for each band in the AOD (1.0-5.0) range of Table 3. Here, the coefficient α of the NIR band (MS4) showed the lowest rate of change (about 27%) in the AOD (2.5-3.0) interval (Fig. 10(a)). In consideration of this rate of change, the AOD interval in Table 3 was optimized that the coefficients α and β for each band can show a rate of change of about 15% within the AOD (1.0-5.0) range. As a result, these LUTs for each band have different AOD intervals (Total number of AODs in MS1: 34, MS2: 32, MS3: 28, MS4: 27). In addition, the DNN model based on Table 3 tended

to be estimated as one value when the change in the input data is small and the change in the output value is small during the training process (Fig. 11 (a)). This optimized LUT-based DNN model solves this problem (Fig. 11(b)). A DNN model was generated based on this optimized LUT, and an interpolation method was applied to this optimized LUT.



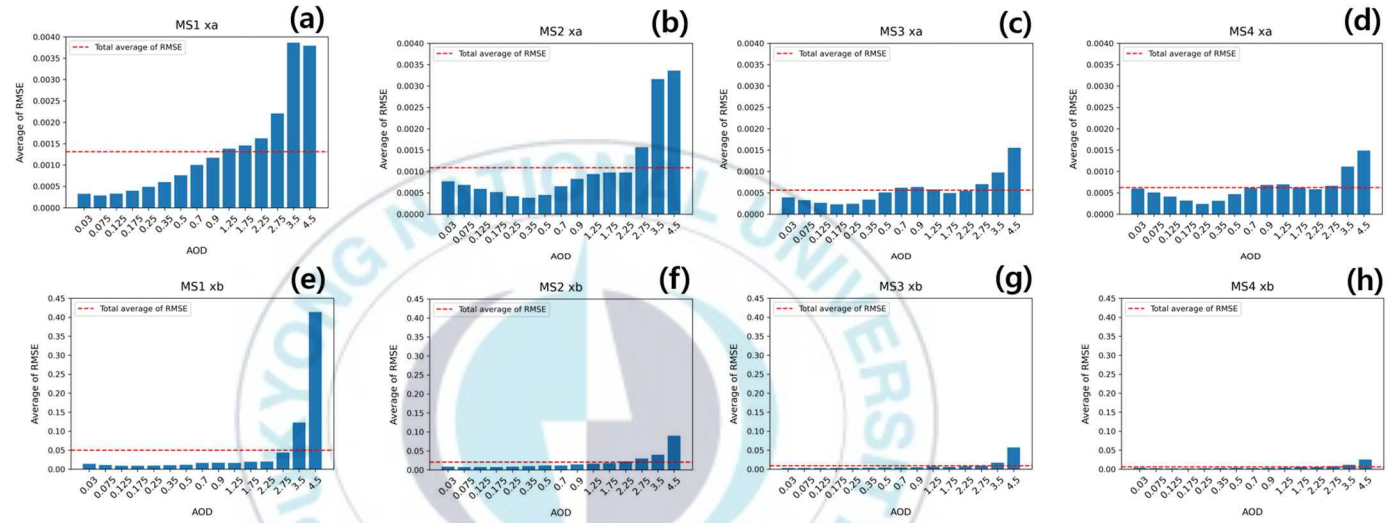


Fig. 9. The average of RMSE for coefficients xa , xb of each band based on DNN. MS1 ((a), (e)), MS2 ((b), (f)), MS3 ((c), (g)), MS4 ((d), (h)) bands. The first and second rows represent the coefficients xa and xb , respectively.

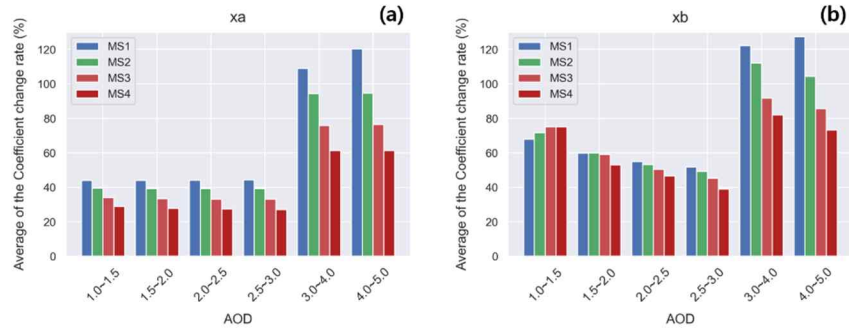


Fig. 10. The rate of change of coefficients x_a and x_b for each band in the AOD (1.0-5.0) range in Table 3. (a) The rate of change of coefficients x_a , (b) the rate of change of coefficients x_b

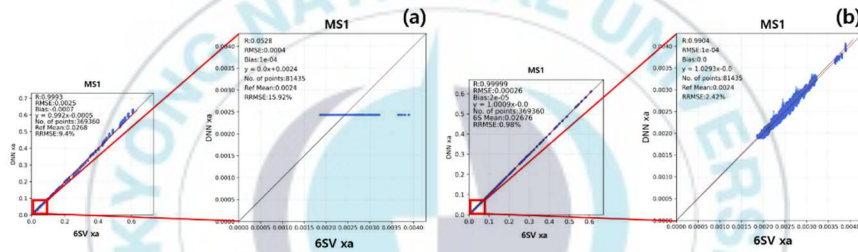


Fig. 11. (a) Table 3 based DNN model estimation results, (b) optimized LUT based DNN model estimation results

4.2. Evaluation of the DNN model

To evaluate the estimation accuracy of the optimized LUT-based DNN model, LUT and interpolated LUT (MCS, 6D) were used. Reference data for comparative analysis are the coefficients α and β of 6SV calculated by simulating the condition of Table 5. Fig. 12, Fig. 13, Fig. 14, and Fig. 15 show the accuracy of DNN, LUT, MCS and 6D calculated for the coefficient α of 6SV, respectively. Fig. 15, Fig. 16, Fig. 17, and Fig. 18 shows the accuracy for the coefficient β . Because of the interval of the input parameters, the error of the LUT increases as the coefficient value to be calculated increases. In MCS, SZA and AOD were interpolated, so the error caused by the interval was relatively reduced compared to the LUT. However, since there are input parameters that have not been interpolated, the error increases as the coefficient value to be calculated increases. 6D showed higher accuracy than LUT and MCS because linear interpolation was applied to all input parameters. DNN showed lower RMSE and RRMSE than 6D in all bands. The accuracy of each method calculated by RMSE and RRMSE is shown in Table 6 and Table 7.

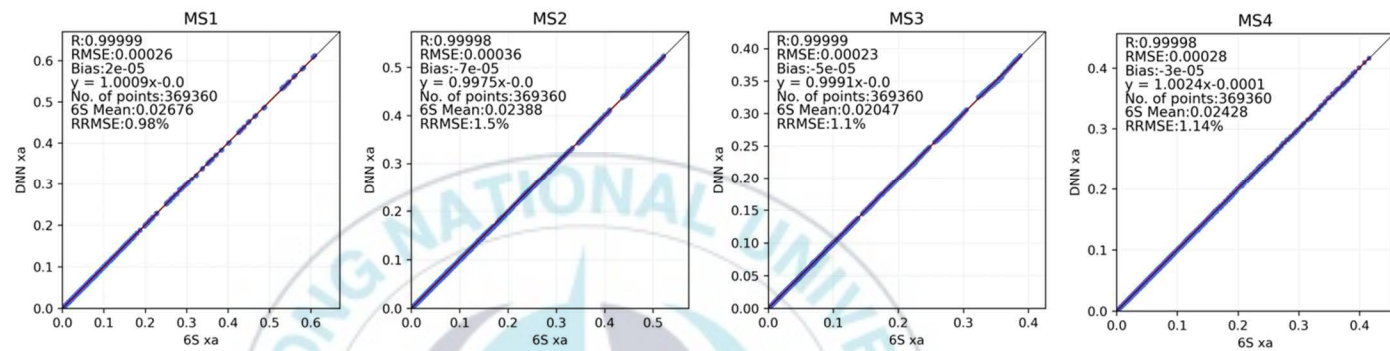


Fig. 12. Scatter plot of DNN x_a and 6SV x_a for each band.

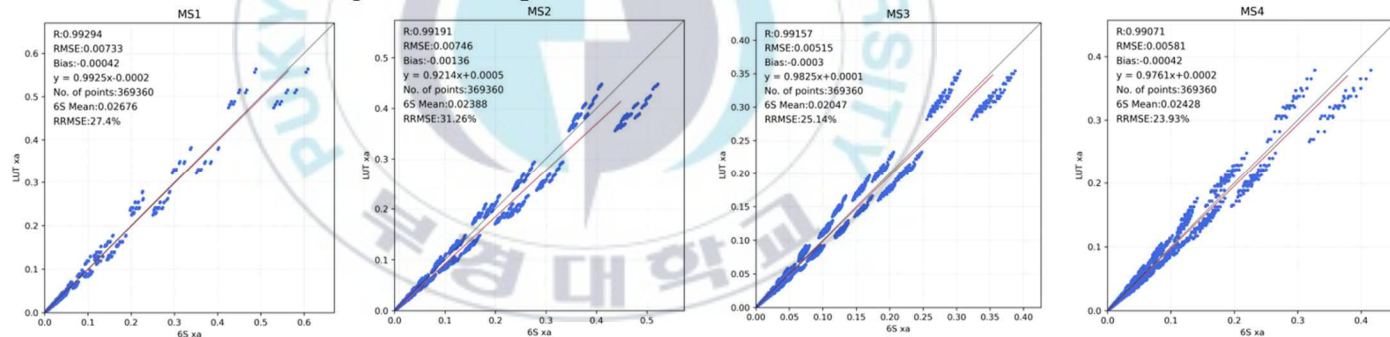


Fig. 13. Scatter plot of LUT x_a and 6SV x_a for each band.

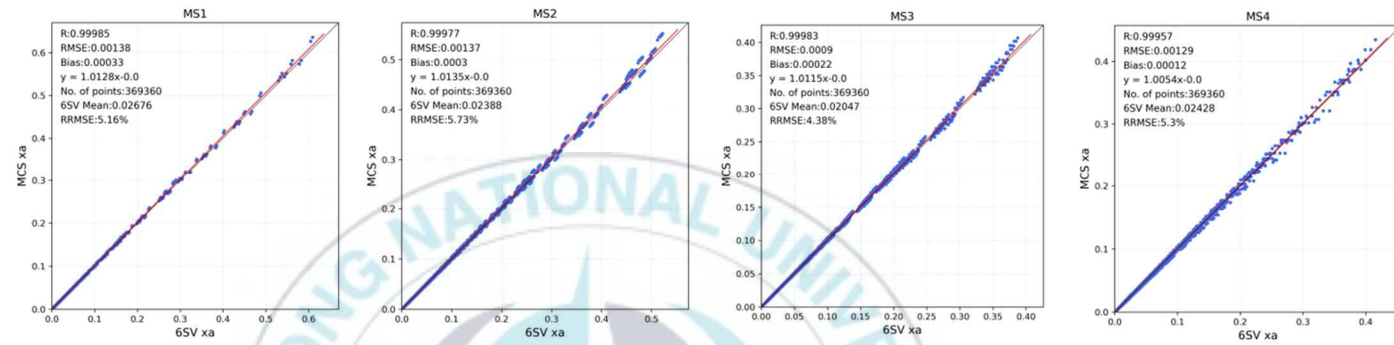


Fig. 14. Scatter plot of MCS x_a and 6SV x_a for each band.

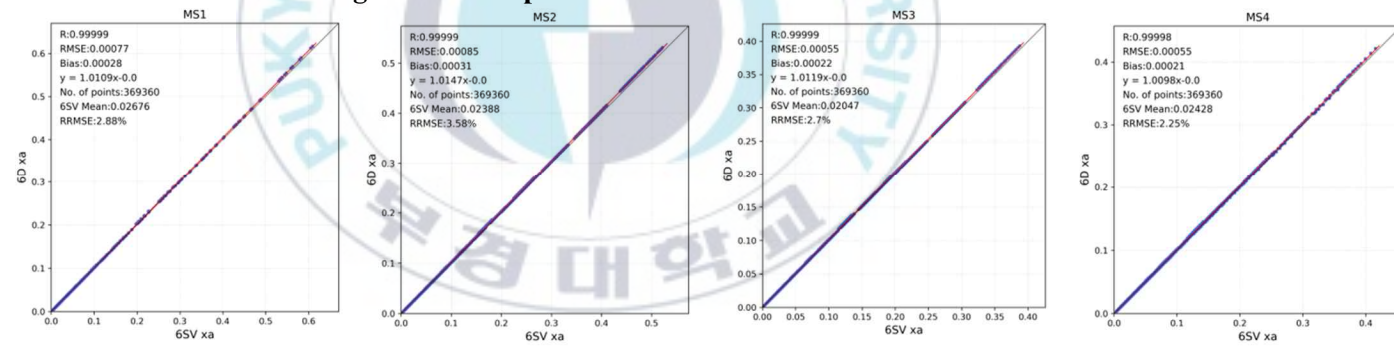


Fig. 15. Scatter plot of 6D x_a and 6SV x_a for each band.

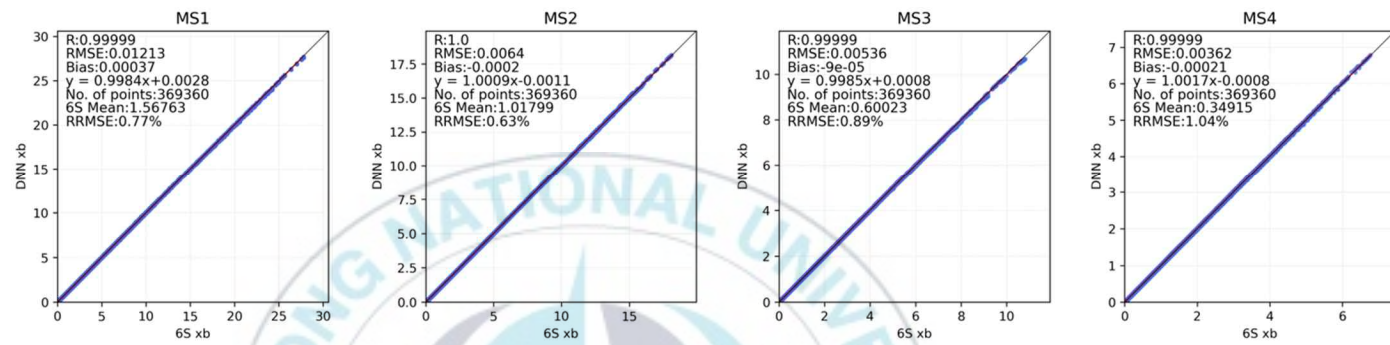


Fig. 16. Scatter plot of DNN xb and 6SV xb for each band.

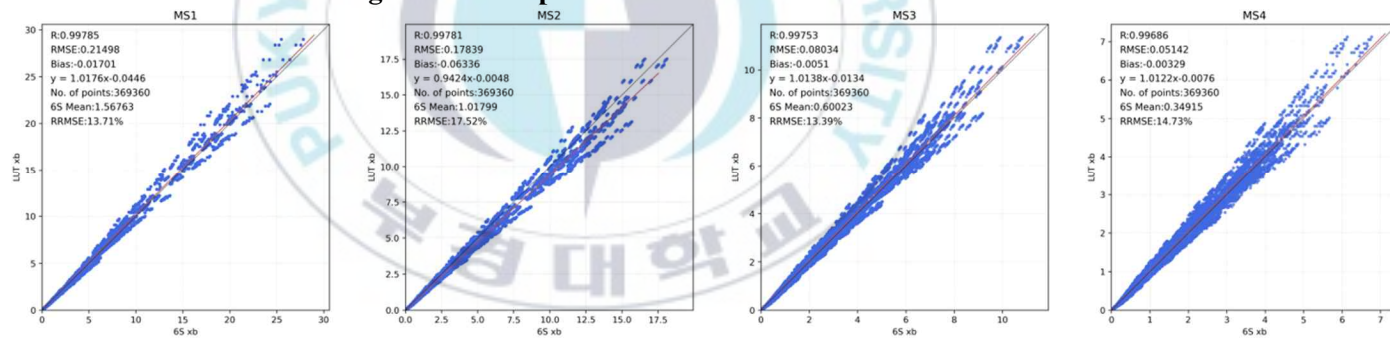


Fig. 17. Scatter plot of LUT xb and 6SV xb for each band.

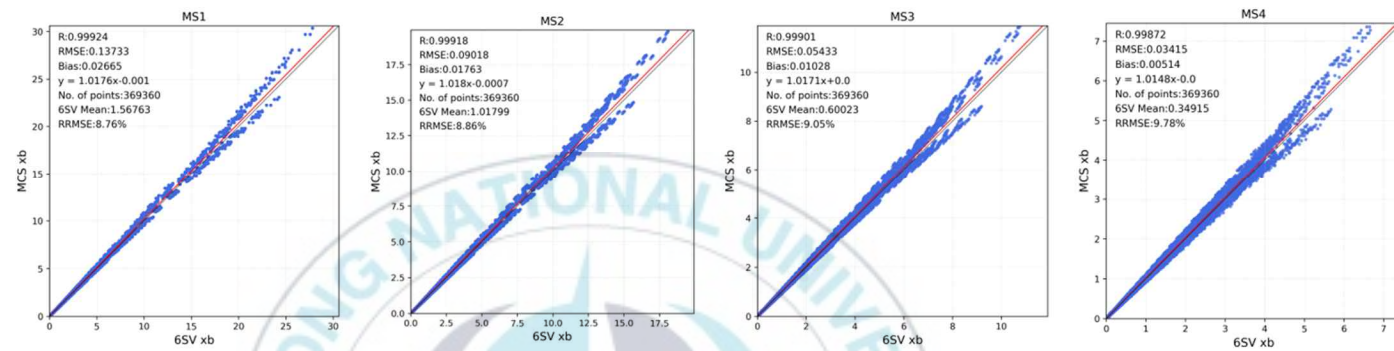


Fig. 18. Scatter plot of MCS xb and 6SV xb for each band.

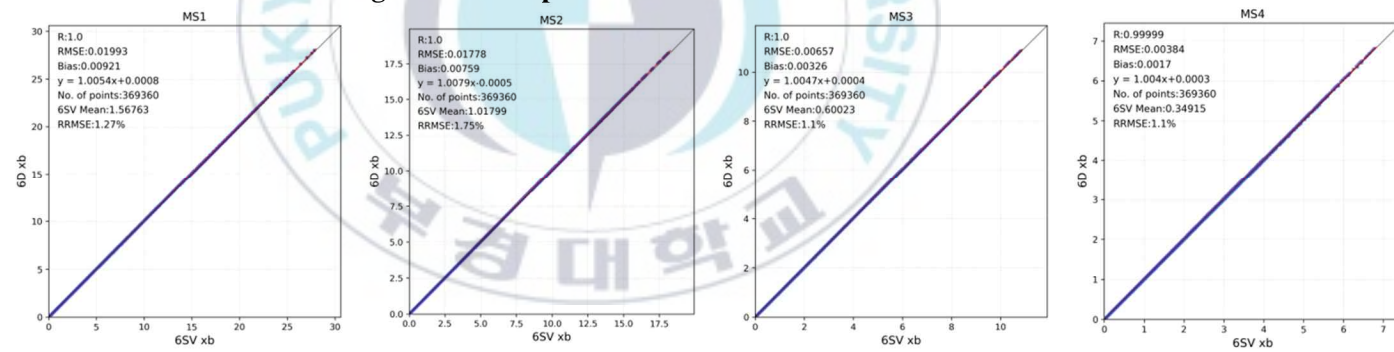


Fig. 19. Scatter plot of 6D xb and 6SV xb for each band

Table 6. DNN, LUT, MCS, and 6D accuracy evaluation for coefficients of each band.

RMSE	MS1		MS2		MS3		MS4	
	<i>xa</i>	<i>xb</i>	<i>xa</i>	<i>xb</i>	<i>xa</i>	<i>xb</i>	<i>xa</i>	<i>xb</i>
DNN	0.0003	0.0121	0.0004	0.0064	0.0002	0.0054	0.0003	0.0036
LUT	0.0073	0.2150	0.0075	0.1784	0.0051	0.0803	0.0058	0.0514
MCS	0.0014	0.1373	0.0014	0.0902	0.0009	0.0543	0.0013	0.0341
6D	0.0008	0.0199	0.0009	0.0178	0.0006	0.0066	0.0006	0.0038

Table 7. DNN, LUT, MCS, and 6D accuracy evaluation for coefficients of each band.

RRMSE (%)	MS1		MS2		MS3		MS4	
	<i>xa</i>	<i>xb</i>	<i>xa</i>	<i>xb</i>	<i>xa</i>	<i>xb</i>	<i>xa</i>	<i>xb</i>
DNN	1.0	0.8	1.5	0.6	1.1	0.9	1.1	1.0
LUT	27.4	13.7	31.3	17.5	25.1	13.4	23.9	14.7
MCS	5.2	8.8	5.7	8.9	4.4	9.1	5.3	9.8
6D	2.9	1.3	3.6	1.8	2.7	1.1	2.3	1.1

4.3. Evaluation of surface reflectance

4.3.1. Accuracy comparison

Table 8 shows the average of the RMSE for the surface reflectance of DNN, LUT, MCS, and 6D compared to the 6SV surface reflectance for Fig. 8. The RMSE of the LUT ranged from 0.051-0.209, showing the highest RMSE among the four surface reflectance calculation methods. Next, the RMSE of the MCS interpolated for SZA and AOD was in the range of 0.018-0.068. 6D shows the highest accuracy in all channels. However, the difference between the RMSE of DNN and the RMSE of 6D appears in the range of 0.001-0.005, which is a very small difference. In addition, RMSE was evaluated based on the input parameters (SZA, AOD) that have a great influence on the calculation of surface reflectance.

Fig. 20 shows the RMSE of the surface reflectance according to the SZA interval for each channel. The RMSE of the surface reflectivity calculated from the LUT is increasing significantly in the range of SZA (60° - 80°). The ranges of RMSE appearing at $SZA > 60^{\circ}$ for each channel were 0.27-0.52 (Blue), 0.18-0.33 (Green), 0.10-0.18 (Red), and 0.07-0.11 (NIR). In the range of SZA (70° - 74°), since the LUT was constructed at intervals of 2° , it decreased from the RMSE shown in the range of SZA (65° - 70°) but increased again due to the large change in the range of SZA

(74°-80°). In the case of MCS, the interval of SZA was interpolated with 0.5° intervals, resulting in less RMSE than LUT (Bule: 0.12-0.19, Green: 0.08-0.13, Red: 0.05-0.08, NIR: 0.03-0.05; range of SZA from 70°-80°). However, like LUT, RMSE increases as SZA increases. DNN (Bule: 0.038-0.074, Green: 0.027-0.032, Red: 0.018-0.029, NIR: 0.009-0.017) and 6D (Bule: 0.019-0.041, Green: 0.016-0.035, Red: 0.015-0.026, NIR: 0.006-0.013) show low RMSE in the range of SZA (70°-80°). 6D showed less RMSE than DNN, but there was no significant difference. And, 6D increased RMSE in the SZA (65°-70°) range. This is judged because of the linear interpolation not reflecting the change of the coefficients that change in the form of an exponential function.

Fig. 21 shows the RMSE of the surface reflectance according to the AOD interval for each channel. It appears like the change shown in Fig. 22. The LUT has a significant increase in RMSE (Bule: 0.17-0.42, Green: 0.12-0.26, Red: 0.08-0.14, NIR: 0.06-0.08) in the AOD range (3.0-5.0). On the other hand, MCS was found to be significantly reduced than RMSE in LUT because AOD was interpolated at 0.05 intervals (Bule: 0.06-0.14, Green: 0.04-0.09, Red: 0.03-0.05, NIR: 0.02-0.03; range of AOD from 3.0-5.0). DNN (Bule: 0.030-0.062, Green: 0.028-0.042, Red: 0.019-0.023, NIR: 0.009-0.014) and 6D (Bule: 0.025-0.053, Green: 0.020-0.038, Red: 0.014-0.026, NIR: 0.008-0.013) RMSE

did not appear significantly, and there was no significant difference from each other in the range of AOD (3.0-5.0).

Table 8. Average of RMSE for surface reflectance of each channel based on DNN, LUT, MCS, 6D

RMSE	MS1	MS2	MS3	MS4
DNN	0.033	0.025	0.015	0.009
LUT	0.209	0.131	0.074	0.051
MCS	0.068	0.047	0.029	0.018
6D	0.027	0.020	0.014	0.008



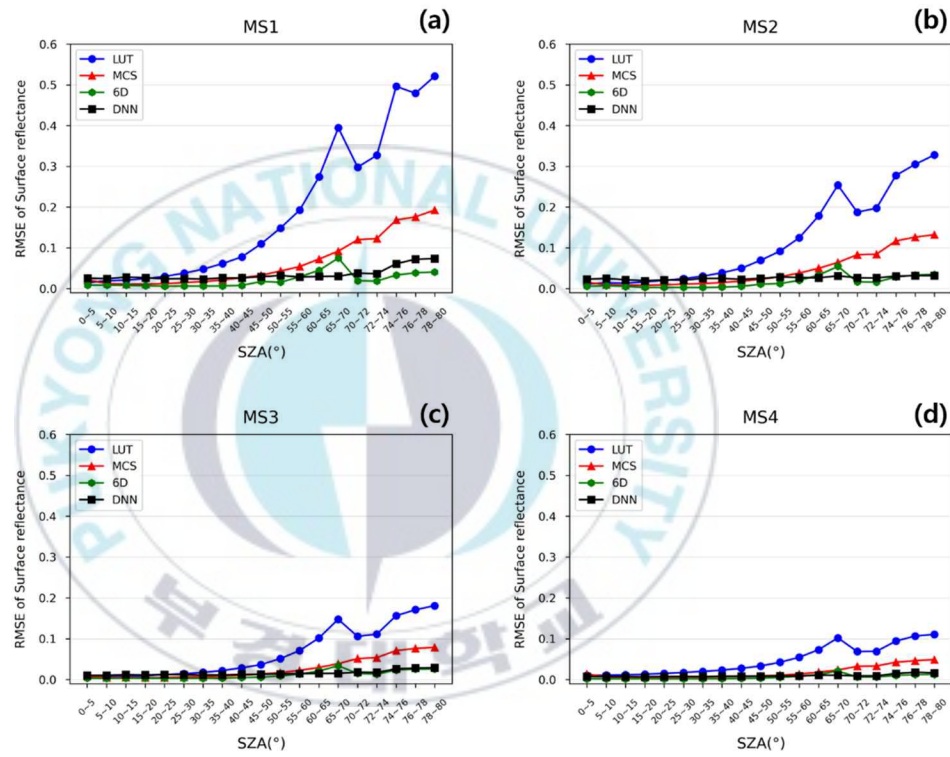


Fig. 20. Average of RMSE for surface reflectance of DNN, LUT, MCS, 6D according to SZA interval. (a) Blue, (b) Green, (c) Red, (d) NIR bands.

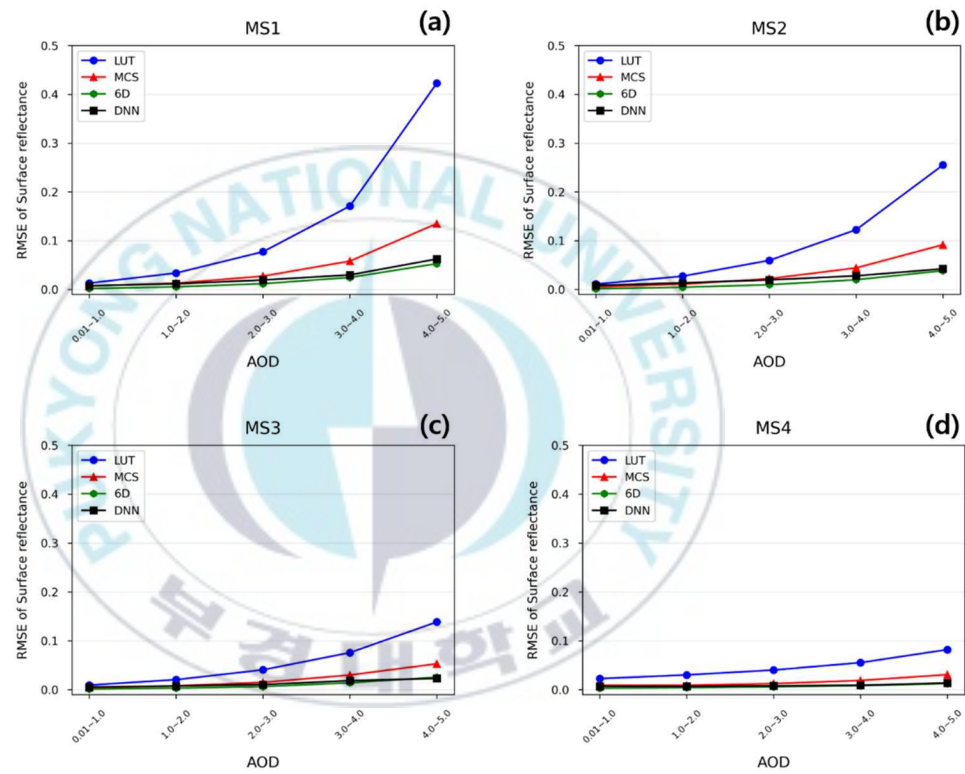


Fig. 21. Average of RMSE for surface reflectance of DNN, LUT, MCS, 6D according to AOD interval. (a) Blue, (b) Green, (c) Red, (d) NIR bands.

4.3.2. Calculation speed comparison

The calculation speed of each method was analyzed by checking the time required to calculate the surface reflectance for each SZA interval. These are the times measured when calculating for the random conditions shown in Fig. 8. The calculation environment is the same for 6SV, LUT, MCS, 6D (Intel (R) Xeon (R) CPU E5-2697 v3 @ 2.60GHz) excluding DNN (Tesla V100-SXM2, 16GB). The calculation of 6SV becomes more complex as SZA increases, so it takes a lot of time to calculate the surface reflectance (from 3206 second to 14400 second). On the other hand, DNN (0.3 second), LUT (0.018 second), MCS (0.13 second), and 6D (18 second) showed a constant calculation speed even when the SZA increased.

In addition, the time required to calculate the surface reflectance for one band from KOMPSAT-3/3A satellite images by each method was analyzed (Table 9). Here, the atmospheric components, angular information for each pixel is given. The surface reflectance was quickly calculated in the order of LUT, MCS, DNN, 6D, and 6SV. 6D and 6SV are not methods that can calculate the surface reflectance of satellite images in real time. Compared to DNN (8.4 second), it was found that the calculation speed of LUT (5.4 second) and MCS (7.1 second) was faster, but this difference does not seem to have a great influence on calculating surface reflectance in real time.

Table 9. Time it takes to calculate surface reflectance from one satellite imagery of 6SV, DNN, LUT, MCS, 6D

Method	6SV	DNN	LUT	MCS	6D
Calculation time (second)	139E+5	8.4	5.4	7.1	84,600

4.3.3. Analysis of discontinuities

Fig. 22 shows the continuity of coefficients xa , xb , and surface reflectance for each band according to SZA (RAA: 90°; VZA: 15°; TPW: 1.5 g/cm²; TCO: 0.3 atm-cm; AOD: 1.0). It was confirmed that all methods except for the LUT were similar to 6SV by removing the discontinuity caused by the LUT interval. In the LUT, in the SZA (0°-60°) range, the effect due to the interval was small, so the discontinuity was not large. In the SZA (60°-80°) range, the discontinuity of the LUT coefficients xa and xb increased, which influenced the occurrence of discontinuity in the surface reflectance. In addition, the SZA (70°-80°) range is constructed with 2° interval, unlike the SZA (60°-70°) range, which is constructed with 5° interval. This has been shown to reduce the size of the discontinuities. However, since this is ineffective for LUT construction and use, it is effective to apply a method that can reflect the variability of coefficients according to the LUT interval.

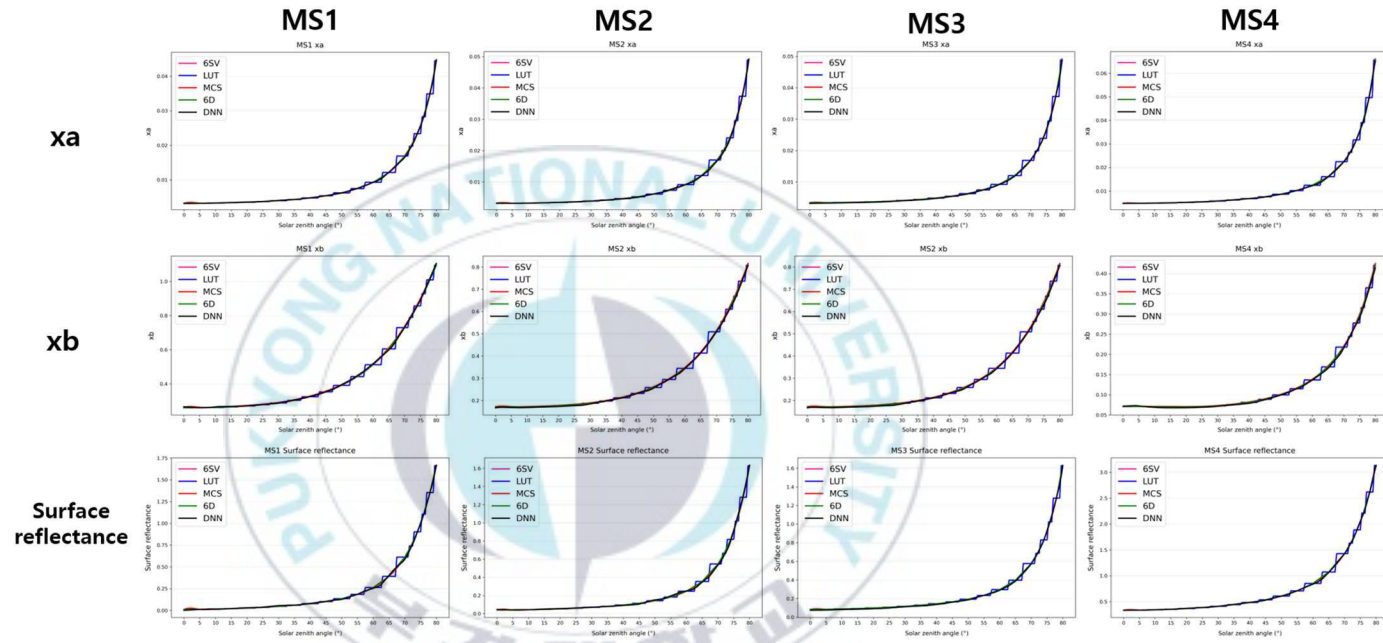


Fig. 22. Analysis of discontinuity of x_a , x_b , and surface reflectance for each channel according to SZA.

5. Summary and Conclusions

Atmospheric correction is an important process to calculate surface reflectance by removing atmospheric effects. To remove the discontinuity, which is the limitation of the existing LUT, a model that calculates the surface reflectance using DNN was generated and evaluated. The LUT was optimized through the sensitivity analysis of the LUT, and the performance of the DNN model was improved based on this optimized LUT. After that, comparative analysis with the LUT interpolation methods used in previous studies was performed. As a result of comparing with 6SV, DNN showed better performance than other interpolation methods. The RMSE was found to be 0.009-0.033 without significant error for various atmospheric components and angular information. In addition, DNN has been shown to calculate the variability of surface reflectance with high accuracy compared to LUT and MCS, which have not been able to resolve the variability of surface reflectance as SZA and AOD increase. And, to calculate the real-time surface reflectance of the satellite image, the calculation speed of each method was compared. The time to calculate the surface reflectance for satellite images did not differ significantly from that of LUT and MCS. DNN differed from LUT and MCS by 1-3 seconds

in calculation speed. That is, the DNN-based atmospheric correction model calculates the surface reflectivity that is not significantly different from 6SV and is a model capable of calculating the real-time surface reflectance from satellite images. In addition, when performing atmospheric correction of high-resolution images, it is possible to calculate precise surface reflectivity based on DNN.



6. References

- Al-Jarrah, O. Y., P. D. Yoo, S. Muhaidat, G. K. Karagiannidis, and K. Taha, 2015. Efficient machine learning for big data: A review, *Big Data Research*, 2(3), 87-93.
- Berk, A., G. P. Anderson, P. K. Acharya, L. S. Bernstein, L. Muratov, J. Lee, M. Fox, S. M. Adler-Golden, J. H. Chetwynd Jr, M. L. Hoke, R. B. Lockwood, J. A. Gardner, T. W. Cooley, C. C. Borel, P. E. Lewis, and E. P. Shettle, 2006. MODTRAN5: 2006 update, *In Algorithms and Technologies for Multispectral, Hyperspectral, and Ultraspectral Imagery XII*, Vol. 6233, p. 62331F. International Society for Optics and Photonics.
- Boehmler, J. M., S. M. Loria-Salazar, C. Stevens, J. D. Long, A. C. Watts, H. A. Holmes, J. C. Barnard, and W. P. Arnott, 2018. Development of a multispectral albedometer and deployment on an unmanned aircraft for evaluating satellite retrieved surface reflectance over Nevada's Black Rock Desert, *Sensors*, 18(10), 3504.
- Cook, D., 2016. *Practical machine learning with H2O: powerful, scalable techniques for deep learning and AI*. " O'Reilly Media, Inc."
- Corlett, R., 2014, *The ecology of tropical East Asia*, Oxford University Press, USA.

- Guanter, L., R. Richter, and H. Kaufmann, 2009. On the application of the MODTRAN4 atmospheric radiative transfer code to optical remote sensing, *International Journal of Remote Sensing*, 30(6), 1407-1424.
- Ignatov, A. and L. Stowe, 2002. Aerosol retrievals from individual AVHRR channels. Part I: Retrieval algorithm and transition from Dave to 6S radiative transfer model, *Journal of the Atmospheric Sciences*, 59(3), 313-334.
- Kaufman, Y. J., D. Tanré, L. A. Remer, E. F. Vermote, A. Chu, and B. N. Holben, 1997. Operational remote sensing of tropospheric aerosol over land from EOS moderate resolution imaging spectroradiometer, *Journal of Geophysical Research: Atmospheres*, 102(D14), 17051-17067.
- Kotchenova, S. Y., E. F. Vermote, R. Matarrese, and F. J. Klemm Jr, 2006. Validation of a vector version of the 6S radiative transfer code for atmospheric correction of satellite data. Part I: Path radiance, *Applied optics*, 45(26), 6762-6774.
- Krizhevsky, A., I. Sutskever, and G. E. Hinton, 2017. Imagenet classification with deep convolutional neural networks, *Communications of the ACM*, 60(6), 84-90.
- Lee, C. S., J. M. Yeom, H. L. Lee, J. J. Kim, and K. S. Han, 2015. Sensitivity analysis of 6S-based look-up table for surface reflectance

- retrieval, *Asia-Pacific Journal of Atmospheric Sciences*, 51(1), 91-101.
- Lee, K. S., C. S. Lee, M. Seo, S. Choi, N. H. Seong, D. Jin, J. M. Yeom, and K. S. Han, 2020. Improvements of 6S Look-Up-Table Based Surface Reflectance Employing Minimum Curvature Surface Method, *Asia-Pacific Journal of Atmospheric Sciences*, 1-14.
- Liang, S., H. Fang, and M. Chen, 2001. Atmospheric correction of Landsat ETM+ land surface imagery. I. Methods, *IEEE Transactions on geoscience and remote sensing*, 39(11), 2490-2498.
- Liang, S., D. Wang, T. He, and Y. Yu, 2010. GOES-R Advanced Baseline Imager (ABI) algorithm theoretical basis document for surface albedo, *NOAA NESDIS CENTER for SATELLITE APPLICATIONS and REARCH*.
- Liang, S., B. Zhong, and H. Fang, 2006. Improved estimation of aerosol optical depth from MODIS imagery over land surfaces, *Remote Sensing of Environment*, 104(4), 416-425.
- Lyapustin, A., J. Martonchik, Y. Wang, I. Laszlo, and S. Korkin, 2011. Multiangle implementation of atmospheric correction (MAIAC): 1. Radiative transfer basis and look-up tables, *Journal of Geophysical Research: Atmospheres*, 116(D3).
- Ma, R., H. Letu, K. Yang, T. Wang, C. Shi, J. Xu, J. Shi, C. Shi, and L.

- Chen, 2020. Estimation of surface shortwave radiation from Himawari-8 satellite data based on a combination of radiative transfer and deep neural network, *IEEE Transactions on Geoscience and Remote Sensing*.
- Mayer, B., and A. Kylling, 2005. The libRadtran software package for radiative transfer calculations? description and examples of use.
- Meyer, K., S. Platnick, G. T. Arnold, R. E. Holz, P. Veglio, J. Yorks, and C. Wang, 2016. Cirrus cloud optical and microphysical property retrievals from eMAS during SEAC4RS using bi-spectral reflectance measurements within the 1.88 μm water vapor absorption band, *Atmospheric measurement techniques*, 9(4), 1743.
- Qu, Y., Q. Liu, S. Liang, L. Wang, N. Liu, and S. Liu, 2013. Direct-estimation algorithm for mapping daily land-surface broadband albedo from MODIS data, *IEEE Transactions on Geoscience and Remote sensing*, 52(2), 907-919.
- Rabah, M. and M. Kaloop, 2013. The use of minimum curvature surface technique in geoid computation processing of Egypt, *Arabian journal of geosciences*, 6(4), 1263-1272.
- Schmidhuber, J., 2015. Deep learning in neural networks: An overview, *Neural networks*, 61, 85-117.
- Staenz, K., R. A. Neville, S. Clavette, R. Landry, H. P. White, and R.

- Hitchcock, 2002. Retrieval of surface reflectance from Hyperion radiance data, *In IEEE International Geoscience and Remote Sensing Symposium*, Vol. 3, pp. 1419-1421. IEEE.
- Thomas, J., S. Thomas, and L. Sael, 2017. Feature versus raw sequence: Deep learning comparative study on predicting pre-mirna, *arXiv preprint arXiv:1710.06798*.
- Vermote, E. F. T. D., D. Tanré, J. L. Deuzé, M. Herman, J. J. Morcrette, and S. Y. Kotchenova, 2006. Second simulation of a satellite signal in the solar spectrum-vector (6SV), *6S User Guide Version*, 3(2), 1-55.
- Vermote, E. F., S. Y. Kotchenova, and J. P. Ray, 2011. MODIS surface reflectance user's guide, *MODIS Land Surface Reflectance Science Computing Facility, version, 1*.
- Vermote, E. F., D. Tanré, J. L. Deuze, M. Herman, and J. J. Morcette, 1997. Second simulation of the satellite signal in the solar spectrum, 6S: An overview, *IEEE transactions on geoscience and remote sensing*, 35(3), 675-686.
- Vu, T. T. and Y. Ban, 2010. Context-based mapping of damaged buildings from high-resolution optical satellite images, *International Journal of Remote Sensing*, 31(13), 3411-3425.
- Wang, X., J. Huang, M. Ji, and K. Higuchi, 2008. Variability of East Asia

dust events and their long-term trend, *Atmospheric Environment*, 42(13), 3156-3165.

Yeom, J. M., J. Ko, J. Hwang, C. S. Lee, C. U. Choi, and S. Jeong, 2018. Updating absolute radiometric characteristics for KOMPSAT-3 and KOMPSAT-3A multispectral imaging sensors using well-characterized pseudo-invariant tarps and microtops II, *Remote Sensing*, 10(5), 697.

Yeom, J. M., S. Park, T. Chae, J. Y. Kim, and C. S. Lee, 2019. Spatial assessment of solar radiation by machine learning and deep neural network models using data provided by the COMS MI geostationary satellite: A case study in South Korea, *Sensors*, 19(9), 2082.

